Analysis of electron transport in a two-dimensional structure using quantal trajectories

1998 J. Phys.: Condens. Matter 10 5583

(http://iopscience.iop.org/0953-8984/10/25/010)

J. Phys.: Condens. Matter **10** (1998) 5583–5594. Printed in the UK PII: S0953-8984(98)88497-X

Analysis of electron transport in a two-dimensional structure using quantal trajectories

Tomas Lundberg†§, Erik Sjöqvist‡‖ and Karl-Fredrik Berggren†¶

† Department of Physics and Measurement Technology, Linköping University, S-581 83 Linköping, Sweden

‡ Sub-Faculty of Philosophy, Oxford University, 10 Merton Street, Oxford OX1 4JJ, UK

Received 16 October 1997, in final form 20 April 1998

Abstract. Ballistic and dissipative electron transport through a two-dimensional geometry is studied in the de Broglie–Bohm quantal trajectory model. The dissipative effect, incorporated to simulate inelastic scattering, is introduced via an imaginary potential term in the Hamiltonian. The relation between the conductance and the local behaviour of the quantal trajectories is discussed. The vortex-like structure of the de Broglie–Bohm trajectories in the vicinity of wavefunction nodes is studied.

1. Introduction

The progress in modern semiconductor technology has made it possible to design nanostructure devices where mobile electrons are confined in one or several directions. For example, a quantum well can be created at a GaAs/AlGaAs interface, trapping the electrons in a sheet with a thickness of the order of 100 Å. The confinement causes a quantization of the energy levels in the direction perpendicular to the interface, and a (quasi-) two-dimensional electron gas is formed. At low temperatures, usually only the lowest-energy subband is populated. In the plane of the interface it is then possible to achieve mean free paths of the order of micrometres, which means that the electrons move ballistically [1–3].

By applying lithographic techniques, e.g., split gates, it is possible to reduce the dimensionality even further and create (quasi-) one-dimensional channels or (quasi-) zero-dimensional dots. When the length of the channel is less than the mean free path, the electrons maintain their phase coherence through the system. Experimentally, it was discovered independently by Wharam *et al* [4] and van Wees *et al* [5] that the conductance through a narrow channel connecting two reservoirs is quantized as $G = 2e^2N/h$, where N is the number of occupied one-dimensional subbands in the channel.

The relatively large size of the nanostructures implies that it is sometimes possible to describe the electrons using classical or semiclassical trajectories (see e.g. [6]). These approaches are useful for qualitative studies while quantitative results should be used with some caution since (semi-) classical models might be too simple to accurately describe the system. To overcome this, while still retaining the trajectory concept, one may use the

§ E-mail: tolun@ifm.liu.se.

‖ E-mail: erik.sjoqvist@philosophy.oxford.ac.uk.

¶ E-mail: kfber@ifm.liu.se.

0953-8984/98/255583+12$19.50

de Broglie–Bohm model [7–10], in which the trajectories are directly determined by the Schrödinger solution ψ.

In this paper we analyse the de Broglie–Bohm quantal trajectories in a quantum dot. The aim is to provide a deeper understanding of the global properties, such as the conductance through the dot, by adopting the view that these properties are built up from individual quantum processes. In particular we focus on the vortex-like structure of the trajectories in the vicinity of wavefunction nodes. Furthermore, we study the effects of inelastic scattering introduced via an imaginary potential term in the Hamiltonian. Although it is usually neglected (which is a reasonable approximation when the mean free path is longer than the size of the structure), some inelastic scattering always takes place, and a more realistic treatment of a nanostructure should take this into account [11, 12]. We demonstrate that the de Broglie–Bohm trajectories provide additional physical insights into inelastic scattering, at least in a qualitative way, within the imaginary potential model.

The layout of the paper is as follows. In section 2 we give a short introduction to the de Broglie–Bohm model and how to include inelastic scattering. Section 3 describes the technique for solving the Schrödinger equation, and the results of the numerical calculations are discussed in section 4. Finally, section 5 contains the conclusions.

2. The de Broglie–Bohm model

Let us first recall the elements of the de Broglie–Bohm model [7–10]. A quantal system is assumed to consist of a wave and a particle. The wave is described by the quantum mechanical wavefunction $\psi(\boldsymbol{x}, t)$, which is a solution of the time-dependent Schrödinger equation

$$-\frac{\hbar^2}{2m}\nabla^2\psi + V\psi = \mathrm{i}\hbar\frac{\partial}{\partial t}\psi \tag{1}$$

where $V = V(\boldsymbol{x})$ is the classical potential and m is the mass of the particle. (We consider only one-particle systems and vanishing vector potential.) The particle follows a trajectory $\boldsymbol{X}(t)$ given by the guidance equation

$$m\dot{\boldsymbol{X}} = \boldsymbol{\nabla} S^{\psi}(\boldsymbol{x}, t)\big|_{\boldsymbol{x}=\boldsymbol{X}} \tag{2}$$

where $S^{\psi}/\hbar$ is the phase of ψ and ρ^{ψ} is the normalized probability density fulfilling the continuity equation

$$\frac{\partial \rho^{\psi}}{\partial t} + \boldsymbol{\nabla}\cdot\left(\rho^{\psi}\frac{\boldsymbol{\nabla} S^{\psi}}{m}\right) = 0. \tag{3}$$

The density $\rho^{\psi} = |\psi|^2$ expresses the impossibility of observing the trajectory $\boldsymbol{X}(t)$. We also note that the real part of the Schrödinger equation takes the form of a generalized Hamilton–Jacobi equation:

$$\frac{(\nabla S^{\psi})^2}{2m} + V + Q^{\psi} = -\frac{\partial S^{\psi}}{\partial t} \tag{4}$$

with the so-called 'quantum potential'

$$Q^{\psi} = -\frac{\hbar^2}{2m}\frac{\nabla^2\sqrt{\rho^{\psi}}}{\sqrt{\rho^{\psi}}} \tag{5}$$

accompanying the classical potential V. From this it is possible to deduce the trajectories by appeal to Newton's second law with the 'force' $-\boldsymbol{\nabla}(V + Q^{\psi})$ and the initial velocity given by (2). However, from the calculational side nothing is gained with the use of Newton's

equations, as the guidance equation is both sufficient and simpler to solve to obtain the trajectories.

We emphasize that the structure given by (1) and (2) is highly non-classical. First we note that the motion of the particle is determined only indirectly by the classical potential through the wavefunction. Therefore there is in general no reason to expect any resemblance between the motion determined by (2) and the solution for the corresponding classical Newton's equation. Indeed in the case of a free wave packet the spreading generally causes the particle to deviate from the classical straight-line motion. Secondly the momentum is not an independent variable as it is in classical mechanics: specifying the initial position $\boldsymbol{X}(0)$ is sufficient to completely determine the trajectory. In other words the trajectories in extended configuration space $(\boldsymbol{x}, t)$ cannot cross.

In this work we concentrate the analysis on stationary elastic and inelastic scattering, where the complex-valued wavefunction is a solution of the time-independent Schrödinger equation

$$-\frac{\hbar^2}{2m}\nabla^2\psi + V\psi = E\psi \tag{6}$$

with the energy eigenvalue E. Solutions of (6) give rise to trajectories which can be completely analysed in configuration space $\boldsymbol{x}$ as the velocity field $\boldsymbol{\nabla} S^\psi/m$ is time independent. In the elastic case the potential V is real valued.

The inelastic scattering is simulated by a complex potential of the form $V_R(\boldsymbol{x}) + \mathrm{i}V_I(\boldsymbol{x})$. This models the effect of the inelastic scattering as a randomization of the phase of the scattered electron causing loss of interference. Inserting the complex potential into (6) yields the continuity equation

$$\boldsymbol{\nabla}\cdot\left(\rho^\psi\frac{\boldsymbol{\nabla}S^\psi}{m}\right) = \frac{2\rho^\psi}{\hbar}(V_I - \operatorname{Im}E) \tag{7}$$

and the Hamilton–Jacobi equation

$$\frac{(\nabla S^\psi)^2}{2m} + V_R + Q^\psi = \operatorname{Re}E. \tag{8}$$

From (7) we obtain that if V_I is independent of $\boldsymbol{x}$, then it is possible to choose $\operatorname{Im}E = V_I$ and there is no dissipative effect on the trajectories. On the other hand if the imaginary potential is spatially varying, the velocity $\boldsymbol{\nabla}S^\psi/m$, and hence also the trajectories, are affected, as the right-hand side of (7) does not vanish. This indicates that the argument in [13] for the rejection of an imaginary potential as a model for dissipative effects is generally not correct. Indeed the calculations in section 4, where we make use of a spatially varying imaginary potential (see equation (15)), support this conclusion.

The complex term also gives rise to an imaginary part of the wave vectors in a plane-wave expansion of ψ, which in turn causes exponential damping of $|\psi|^2$. This damping is of the form $\exp(-x/l)$, where l can be regarded as the inelastic mean free path (see [14] and [15], and references therein). In effect, we have introduced a finite inelastic mean free path in our system.

3. Solution of the Schrödinger equation

Our model device is shown in figure 1(a). It consists of two semi-infinite regions connected with a cross-bar structure. If a weak potential difference is applied between the two regions, a current will flow through the cross-bar structure. The length of the structure is of the

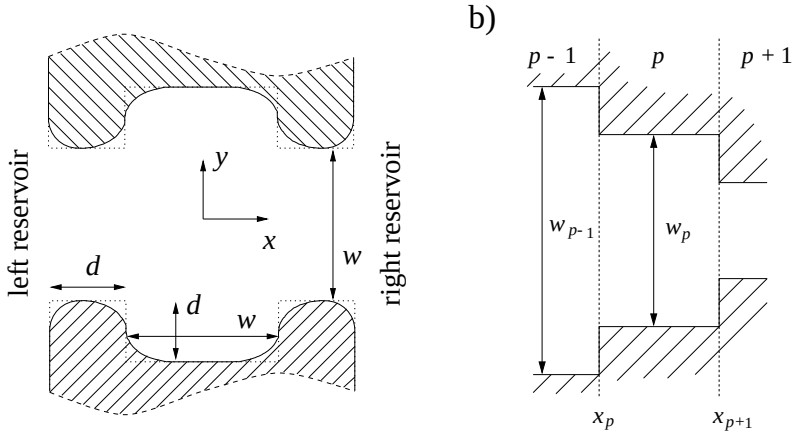

Figure 1. The model device used in the calculations. The potential is zero in the two reservoirs and in the cross-bar structure, and infinite elsewhere. (a) The confining potential in the two-dimensional electron gas. The dotted line shows the gate structure with sharp corners. The actual shape of the confining potential is obtained from this by replacing the sharp corners with smooth, rounded corners. In our calculations, we have used $d = 500$ Å and $w = 1000$ Å. (b) The smooth corners are approximated by dividing the cross-bar into narrow strips. The figure shows the pth strip and its neighbours. The width of the strip is denoted by w_p.

order of 1000 Å which is less than the mean free path of the electron gas. We first neglect inelastic scattering so that the electrons move ballistically through the structure.

The two-dimensional cross-bar structure can be induced by a split-gate confinement technique. It consists in depositing metallic Schottky gates on top of the structure. When the gates are connected to a negative voltage, the regions under the gates are depleted of electrons and the cross-bar geometry is formed.

The gate structure is separated from the electron gas by a distance of 500 to 1000 Å. This means that any sharp features in the gate structure is smoothed out in the electron gas. We include this effect by dividing the central cross-bar structure into N strips and varying their widths and lengths to simulate smooth corners (see figure 1(b)). This is a good approximation if the change in width between two adjacent strips is less than the Fermi wavelength.

Within each strip, we assume that the confining potential for the electrons in the y-direction is an infinite square well. Self-consistent calculations, i.e. solving the Schrödinger and Poisson equations simultaneously [16], show that the confining potential varies from parabolic when there is little or no charge in the structure to a truncated parabola with a flat bottom when charge accumulates in the structure. An infinite square-well potential is therefore a rather accurate approximation when charge has accumulated in the well. Furthermore, the use of the infinite square-well potential makes it possible to solve the Schrödinger equation exactly and obtain analytical solutions, which is a great advantage when dealing with quantal trajectories. For example, it makes it possible to zoom in on interesting features of the trajectories. A more realistic confining potential would probably require numerical algorithms, and this would make it difficult to study the detailed behaviour of the trajectories.

Here we only give an outline of how to solve the Schrödinger equation. A more detailed description is given in [17].

The device is divided into three major regions: the left-hand reservoir ($x < x_0$), which

acts as the source, the cross-bar structure ($x_0 < x < x_N$), and the right-hand reservoir ($x > x_N$), which acts as the drain. We solve the Schrödinger equation separately in the three regions and match the wavefunction and its derivative at the boundaries.

In the left-hand reservoir we write the solution as

$$\psi_{\boldsymbol{k}}^{L} = \exp[\mathrm{i}k_x(x - x_0) + \mathrm{i}k_y y] + \int_{-\infty}^{+\infty} A_L(k'_y)\exp[-\mathrm{i}k'_x(x - x_0) + \mathrm{i}k'_y y]\,\mathrm{d}k'_y \tag{9}$$

where the first term is the incident plane wave, the second term contains the backscattered components with probability amplitude A_L, and $\boldsymbol{k} = k_x\hat{\boldsymbol{x}} + k_y\hat{\boldsymbol{y}}$. The components k_x and k_y are related through $E = \hbar^2\boldsymbol{k}^2/2m^*$, where m^* is the effective mass of the electron. For GaAs–GaAlAs, $m^* = 0.067m_e$, where m_e is the free-electron mass. The same relation holds between k'_x and k'_y. In a similar way, we write the wavefunction in the right-hand reservoir as

$$\psi_{\boldsymbol{k}}^{R} = \int_{-\infty}^{+\infty} A_R(k'_y)\exp[\mathrm{i}k'_x(x - x_N) + \mathrm{i}k'_y y]\,\mathrm{d}k'_y \tag{10}$$

where A_R relates to the probability for transmission.

In the cross-bar structure, we write the wavefunction in the pth strip as

$$\psi_{\boldsymbol{k},p}^{C} = \sum_n \left\{B_{n,p}\exp\left[\mathrm{i}q_{n,p}(x - x_{p-1})\right] + C_{n,p}\exp\left[-\mathrm{i}q_{n,p}(x - x_{p-1})\right]\right\} \times \sin\left[\frac{n\pi}{w_p}\left(y + \frac{w_p}{2}\right)\right] \tag{11}$$

where B and C are expansion coefficients. The sum runs over all sub-levels with energies

$$E_{n,p} = \hbar^2(n\pi/w_p)^2/2m^*.$$

For $E > E_{n,p}$ the longitudinal states are travelling waves with wavenumber $q_{n,p} = [2m^*(E - E_{n,p})/\hbar^2]^{1/2}$ while for $E < E_n$ the solutions become exponential with $\mathrm{i}q_{n,p} = [2m^*(E_{n,p} - E)/\hbar^2]^{1/2}$, i.e. we have used the convention $(-1)^{1/2} = -\mathrm{i}$. Using a transfer matrix method (see [17] and references therein) we find the expansion coefficients B, C, A_L and A_R, and hence the wavefunction in all regions.

We consider the temperature $T = 0$ K and an infinitesimally small potential difference U between the source and the drain, the so-called linear response regime. This means that only electrons in the small energy interval $[E_F - eU, E_F]$ contribute to the current through the structure because of the Pauli principle. We can therefore write the wave vector $\boldsymbol{k}$ as

$$\boldsymbol{k} = \boldsymbol{k}(\phi) = k_F[\cos(\phi)\hat{\boldsymbol{x}} + \sin(\phi)\hat{\boldsymbol{y}}]$$

where ϕ is the angle between the incident wave vector $\boldsymbol{k}$ and the x-axis, and k_F is the Fermi wavenumber.

The probability current density $\boldsymbol{j}^{\psi_{\boldsymbol{k}(\phi)}}$ is now found from

$$\begin{aligned}\boldsymbol{j}^{\psi_{\boldsymbol{k}(\phi)}}(x, y) &= j_x^{\psi_{\boldsymbol{k}(\phi)}}(x, y)\hat{\boldsymbol{x}} + j_y^{\psi_{\boldsymbol{k}(\phi)}}(x, y)\hat{\boldsymbol{y}} \\ &= -\frac{\hbar}{m^*}\left(\mathrm{Re}\left[\psi^*_{\boldsymbol{k}(\phi)}\,\mathrm{i}\,\frac{\partial}{\partial x}\psi_{\boldsymbol{k}(\phi)}\right]\hat{\boldsymbol{x}} + \mathrm{Re}\left[\psi^*_{\boldsymbol{k}(\phi)}\,\mathrm{i}\,\frac{\partial}{\partial y}\psi_{\boldsymbol{k}(\phi)}\right]\hat{\boldsymbol{y}}\right).\end{aligned} \tag{12}$$

The partial conductance G^{part} is obtained by taking the electric current

$$j(\phi) = 2(-e)\int_{-w/2}^{w/2}\mathrm{d}y\; j_x^{\psi_{\boldsymbol{k}(\phi)}}(x_0, y) \tag{13}$$

where the factor 2 takes care of the spin degeneracy, and then dividing $j(\phi)$ by the applied voltage U i.e. $G^{\text{part}} = |j(\phi)|/U$. The conductance, including contributions from all incident waves, is obtained by integrating the electric current over all incoming angles:

$$J = \int_{-\pi/2}^{\pi/2} \mathrm{d}\phi \; j(\phi) \tag{14}$$

and then dividing J by the applied voltage: $G = |J|/U$.

We now take inelastic scattering into account. The effect of the inelastic scattering is introduced phenomenologically via an imaginary potential $\mathrm{i}V_I(x)$ added to the real-valued confining potential. Explicitly $V_I(x)$ is taken to be

$$V_I(x) = \begin{cases} -|V_I| & x_0 < x < x_N \\ 0 & x < x_0 \text{ and } x > x_N \end{cases} \tag{15}$$

with $|V_I|$ a constant which is related to the inelastic scattering time τ_ϕ through $|V_I| = \hbar/(2\tau_\phi)$. This kind of potential has previously been used for related nanostructure geometries [12, 18]. It models scattering due to phonons, electron–electron scattering, etc, in the channel. This choice of potential is computationally convenient and is motivated by the fact that the electrons on average spend more time inside the structure (due to the translational asymmetry introduced by the cross-bar structure) with an increased probability for inelastic scattering as a result. Note also that the form (15) of the imaginary potential circumvents the criticism in [13], as $V_I(x)$ is spatially varying. Within each strip the potential is separable, i.e.

$$V(x, y) = V_x(x) + V_y(y) - \mathrm{i}|V_I|$$

where $V_x(x) = 0$ in this case. We are thus free to let the imaginary potential $\mathrm{i}|V_I|$ be a part of V_x or V_y. We have chosen V_x, since we therefore can retain the simple particle-in-a-box solutions for the y-direction. Thus, equation (11) remains unchanged but the definition of q is now

$$q_{n,p} = [2m^*(E - E_{n,p} + \mathrm{i}|V_I|)/\hbar^2]^{1/2} \tag{16}$$

where E and $E_{n,p}$ are real.

The de Broglie–Bohm trajectories for both zero and non-zero imaginary potential are finally obtained from the guidance equation (2), where the velocity is determined through the relation $\nabla S^{\psi_{k(\phi)}}/m = j^{\psi_{k(\phi)}}/\rho^{\psi_{k(\phi)}}$ by calculating $j^{\psi_{k(\phi)}}$ and $\rho^{\psi_{k(\phi)}}$. Equation (2) is integrated using fourth-order Runge–Kutta methods with an adaptive stepsize.

4. Results

For our structure, the staircase dependence of the conductance on the energy for a narrow channel [4, 5] is replaced by a complex pattern of peaks and dips in the case of a cross-bar structure (a detailed discussion of this can be found in [17]; see also the inset in figure 7, later). Peaks are caused by resonant tunnelling via quasi-bound states in the centre of the cross. In addition there are resonant and anti-resonant peaks which are due to constructive and destructive quantum mechanical interference, respectively. Such (anti-) resonances have also been found in a similar system using a more realistic confining potential [19]. This implies that the main results in our work, which seem to be intimately connected to anti-resonances as we will see, would still be valid in models using more realistic confining potentials. We find that the flow of trajectories is smooth and laminar, except in the vicinity of the anti-resonant dips where there is a transition from laminar to vortex flow. The

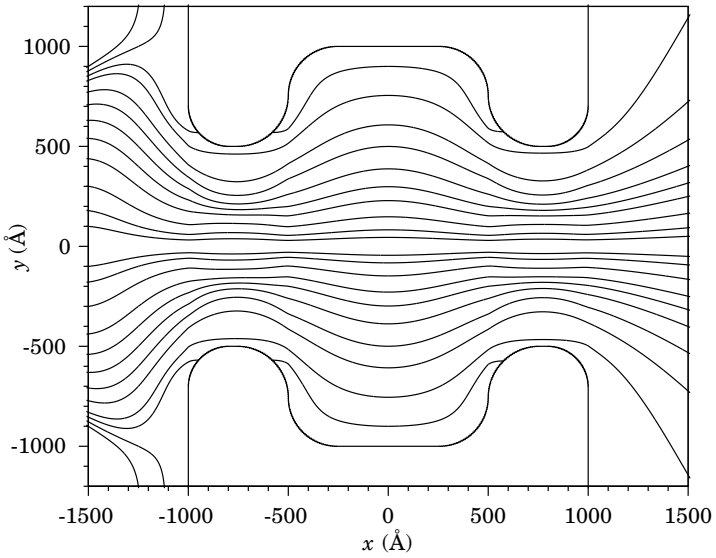

Figure 2. Trajectories at the energy corresponding to the first resonance ($E_F = 0.884\,36$ meV).

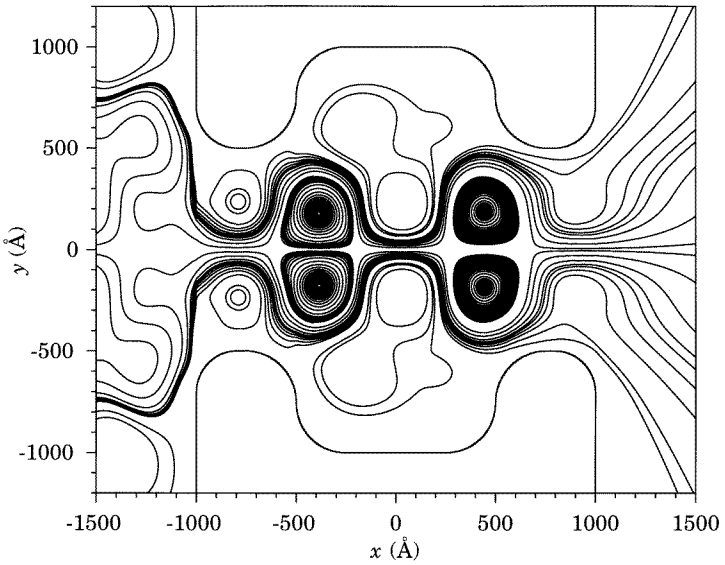

Figure 3. Trajectories at the energy $E_F = 3.750$ meV, approximately 0.011 meV lower than the energy of the third anti-resonance.

complexity of the vortex flow increases with increasing energy. Figure 2 shows the laminar flow at the first resonance ($E_F = 0.884\,36$ meV). Note in particular the formation of trajectories which start and end at the boundary of the dot. In figure 3 the trajectories at $E_F = 3.750$ meV, which is approximately 0.011 meV lower than the energy of the third anti-resonance, are shown. The initial values $\boldsymbol{X}(0)$ are chosen to bring out as many interesting features as possible. Here, and also throughout the rest of this article, the

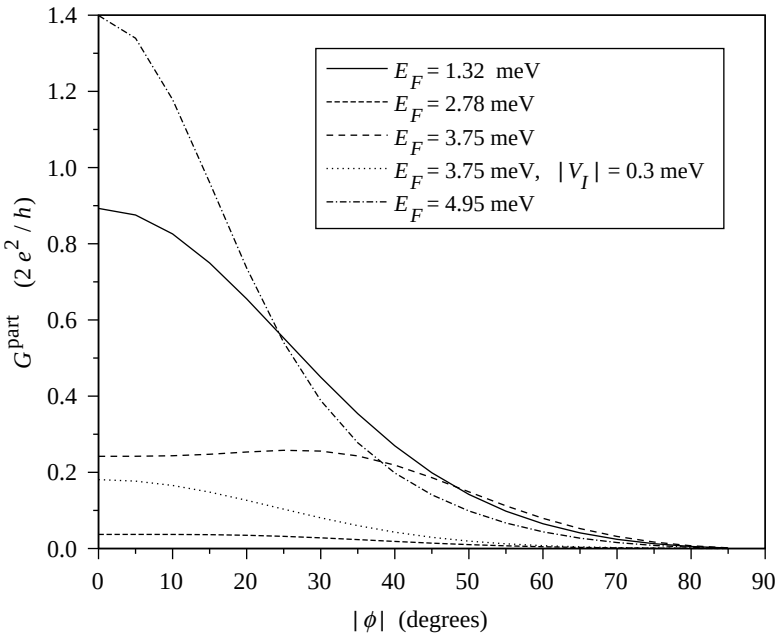

Figure 4. The partial conductance G^{part} plotted as a function of the incoming angle $|\phi|$ (in steps of 5°) for some energies.

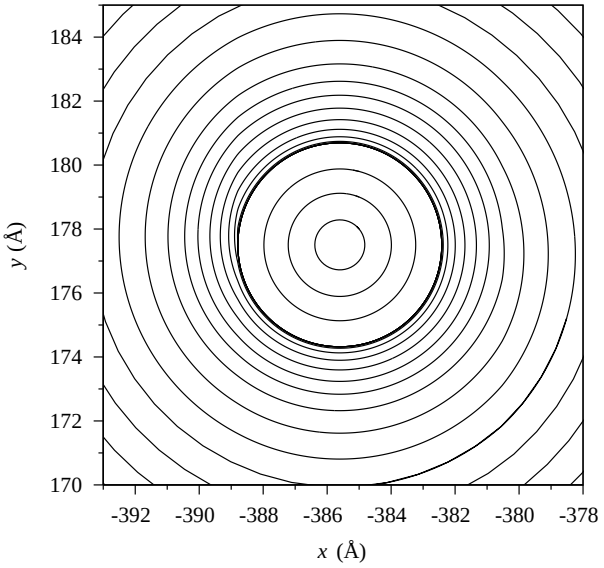

Figure 5. The centre of the vortex centred around $(x, y) \approx (-385$ Å, 178 Å) in figure 3.

incoming wave vector is chosen as $\boldsymbol{k} = k_F\hat{\boldsymbol{x}}$, i.e. $\phi = 0$. The significance of this particular choice of incoming wave is indicated in figure 4 where the partial conductance G^{part} is plotted as a function of the angle $|\phi|$. At energies where the flow is laminar, the partial conductance decreases rather rapidly as $|\phi|$ is increased. For energies with vortex flow,

the partial conductance is practically constant up to $|\phi| \approx 35^\circ$. We have limited ourself to studying just the $\phi = 0$ wave, since it is this particular wave which contributes most to the conductance when the flow is laminar, and we want to study the effect on the trajectories during the transition from laminar to vortex flow. The case of non-zero imaginary potential will be discussed later.

Looking at the trajectories in figure 3, we see that the electrons contributing to the current through the structure are confined to move in two narrow bundles. At the entrance and the exit of the centre of the cross, the electrons are pushed away from the centreline by four vortices, two of them located at $x \approx -385$ Å, $y \approx \pm 178$ Å and the other two at $x \approx 445$ Å, $y \approx \pm 190$ Å. As is shown in figure 5, a closer examination of the vortices reveals that the trajectories form closed circles, demonstrating the circular behaviour close to a node [20–23]. Saddle fixed points [21] are formed at various locations, e.g. at $x \approx -600$ Å, $y = 0$ Å. Note in particular that the stability of the fixed points at the centreline is forced to alternate in the x- and y-directions due to the global structure of the flow.

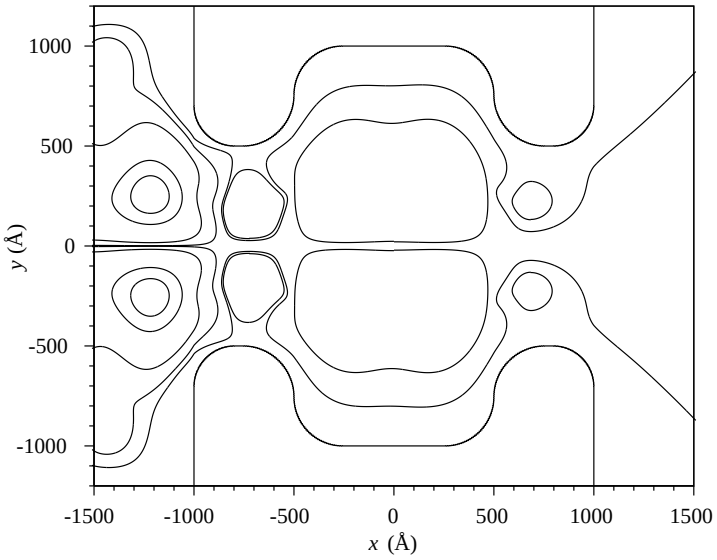

Figure 6. Trajectories at $E_F = 2.780$ meV, approximately 0.024 meV lower than the energy of the second anti-resonance.

At an energy approximately 0.024 meV lower than the energy corresponding to the second anti-resonance (i.e. $E_F = 2.780$ meV), we see the same general picture of quantum vortices blocking the trajectories (see figure 6). The conductance here is very low ($G \sim 0.03 \times 2e^2/h$), and very few trajectories pass through the structure. In general, the reduced conductance at these anti-resonances can be viewed as being due to vortices blocking a large portion of the channel. It is likely that this is a general feature of transport in a nanostructure.

We now turn to a non-trivial imaginary potential $\mathrm{i}V_I(x)$. An intuitive guess is that the partial conductance should decrease for negative imaginary potential in the cross-bar region. In figure 7 we have plotted the partial conductance versus $|V_I|$ for some values of E_F. We see that for energies corresponding to smooth laminar flow, the partial conductance decreases monotonically (solid and dotted lines), as predicted. For energies corresponding to vortex flow, i.e. close to or at the anti-resonances, the partial conductance first decreases

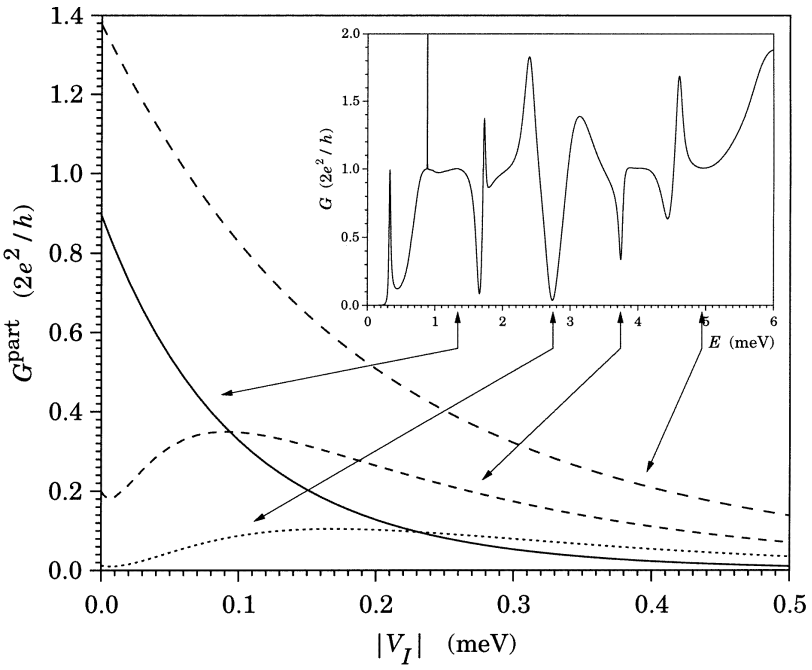

Figure 7. The partial conductance $G^{\rm part}$ versus $|V_I|$, the value of the imaginary potential in the cross-bar region, for some values of E_F. The inset shows the conductance G (including the contributions from all incident waves) at different Fermi energies E_F (in meV) at $T = 0$ K, and is taken from [17].

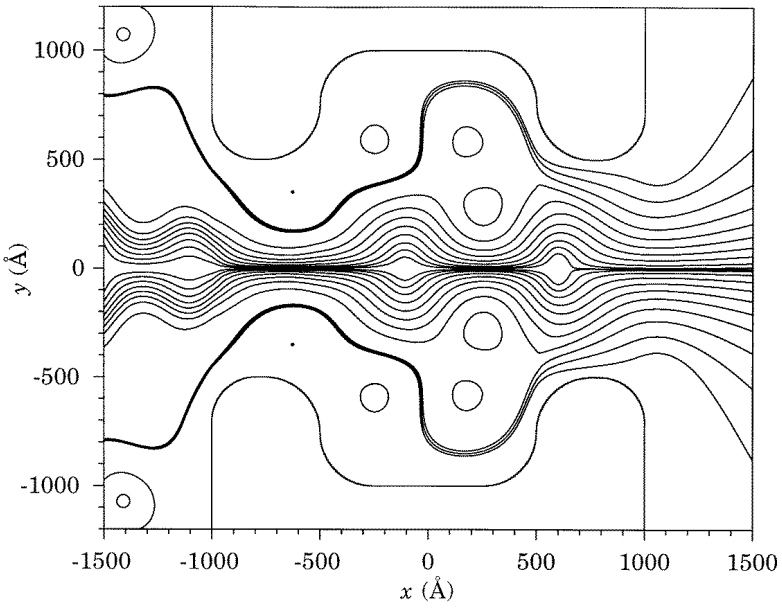

Figure 8. The trajectories for the same energy as in figure 3, but here the imaginary potential in the cross-bar region is non-zero and $|V_I|$ is equal to 0.1 meV. Some of the vortices have disappeared, giving the current-carrying trajectories a straighter path through the structure.

slightly, and this is followed by a significant increase, after which it slowly decreases. This unexpected behaviour can be understood by looking at the trajectories (see figure 8). The vortices have almost disappeared, giving the current-carrying trajectories a shorter and less perturbed path through the structure. That the vortex-like trajectories disappear can, in turn, be understood using the mean free path analogy. Since these trajectories are very long, they exceed the mean free path and the electrons travelling on these trajectories are more likely to be scattered than electrons travelling on shorter trajectories. The effect is that the imaginary potential kills the vortices, giving more room for current-carrying trajectories. Furthermore, we note that the shape of the partial conductance curve as a function of $|\phi|$ in figure 4 takes a Gaussian-like form when the imaginary potential is non-zero, which indicates that the flow has become more laminar also for $|\phi| \neq 0$.

5. Conclusions

We have studied ballistic and dissipative electron transport in a two-dimensional cross-bar structure using the de Broglie–Bohm quantal model. The inelastic scattering has been modelled by a spatially varying imaginary potential. In the calculations of the trajectories we have found striking and highly non-classical features such as the circular structures in the vicinity of a node, and trajectories which start and end at the boundary of the dot. We have also found that the partial conductance for vortex flows initially increases before it starts to decrease when the strength of the imaginary potential increases. This at first sight unexpected behaviour could be explained by noting that the long vortex-like trajectories are more likely to undergo inelastic scattering and therefore are unlikely to appear. Finally, we believe that the physical model used in this paper (the de Broglie–Bohm model with an imaginary potential) provides new insight into the effects of scattering.

Acknowledgments

We wish to thank an anonymous referee for most valuable comments. TL acknowledges financial support from the Swedish Natural Science Research Council. ES acknowledges financial support from The Wenner–Gren Foundation.

References

[1] Ehrenreich H and Turnbull D (ed) 1991 *Semiconductor Heterostructures and Nanosystems (Solid State Physics 44)* (San Diego, CA: Academic)
[2] Reed M (ed) 1992 *Nanostructured Systems (Semiconductors and Semimetals 35)* (San Diego, CA: Academic)
[3] Kelly M J 1995 *Low-Dimensional Semiconductors: Materials, Physics, Technology, Devices* (Oxford: Oxford University Press)
[4] Wharam D A, Thornton T J, Newbury R, Pepper M, Ahmed H, Frost J E F, Hasko D G, Peacock D C, Ritchie D A and Jones G A C 1988 *J. Phys. C: Solid State Phys.* **21** L209
[5] van Wees B J, van Houten H, Beenakker C W J, Williamson J G, Kouwenhoven L P, van der Marel D and Foxon C T 1988 *Phys. Rev. Lett.* **60** 848
[6] Schwieters C D, Alford J A and Delos J B 1996 *Phys. Rev.* B **54** 10 652
[7] de Broglie L 1927 *J. Physique* **5** 225
[8] Bohm D 1952 *Phys. Rev.* **85** 166
Bohm D 1952 *Phys. Rev.* **85** 180
[9] Holland P R 1993 *The Quantum Theory of Motion* (Cambridge: Cambridge University Press)
[10] Bohm D and Hiley B J 1993 *The Undivided Universe* (London: Routledge)
[11] Stone A D and Lee P A 1985 *Phys. Rev. Lett.* **54** 1196
[12] Wang Y, Wang J and Guo H 1993 *Phys. Rev.* B **47** 4348

[13] Spiller T P, Spencer P S, Clarke T D, Ralph J F, Prance H, Prance R J and Clippingdale A 1991 *Found. Phys. Lett.* **4** 507
[14] Knäbchen A 1992 *Phys. Rev.* B **45** 8542
[15] Iannaccone G and Pellegrini B 1996 *Phys. Rev.* B **53** 2020
[16] Laux S E, Frank D J and Stern F 1988 *Surf. Sci.* **196** 101
[17] Lundberg T 1994 *Comput. Mater. Sci.* **3** 78
[18] Akis R, Bird J P and Ferry D K 1996 *J. Phys.: Condens. Matter* **8** L667
[19] Akis R, Vasilopoulos P and Debray P 1997 *Phys. Rev.* B **56** 9594
[20] Hirschfelder J O 1977 *J. Chem. Phys.* **67** 5477
[21] Wu H and Sprung D W L 1993 *Phys. Lett.* **183A** 413
[22] Wu H and Sprung D W L 1994 *Phys. Rev.* **49A** 4305
[23] Wu H and Sprung D W L 1994 *Phys. Lett.* **196A** 229